Wiley
Structural Control and Health Monitoring
Volume 2024, Article ID 5768511, 18 pages
https://doi.org/10.1155/2024/5768511

WILEY

Research Article

Experimental Investigation on Cyclic Performance of Rotation-Based Metallic Damper

Qianqian Li[1], **Jianze Wang**[2], **Tao Li**[2], **Rui Pu**[2], **Jun Xu**[2], **and Kaoshan Dai**[1,2]

[1]*Institute for Disaster Management and Reconstruction, Sichuan University-The Hong Kong Polytechnic University, Chengdu, China*
[2]*Department of Civil Engineering, MOE Key Laboratory of Deep Underground Science, Sichuan University, Chengdu, China*

Correspondence should be addressed to Tao Li; litao52@scu.edu.cn

Received 27 December 2023; Revised 6 April 2024; Accepted 17 June 2024

Academic Editor: Yoshiki Ikeda

Metallic yielding devices have been widely used for improving seismic performance of buildings. However, metallic dampers currently in use are often attached to structural systems through brace components, potentially causing conflicts with architectural requirements. In this study, a metallic damper that utilizes the angular deformation generated at the beam-column connection under lateral loads is proposed. The seismic input energy can be dissipated through inelastic deformations of hyperbolic-shaped steel bars. Firstly, this paper introduces the configuration and design concept of the newly proposed rotation-based metallic damper (RMD). Then, in order to investigate the hysteretic behavior and failure modes of the proposed devices, a total of twelve RMD specimens were fabricated, and quasistatic tests were conducted. Subsequently, the influences of physical characteristics associated with hyperbolic-shaped steel bars on the energy dissipation performance of RMD were studied. Finally, finite element analysis was conducted based on the detailed models of RMD specimens, and the results showed a good agreement with the experimental data. The results demonstrate that the RMD exhibits a sound energy dissipation capacity. It is replaceable and flexible in architectural arrangements due to its low space requirements, which is friendly in engineering practice.

1. Introduction

Earthquakes have been responsible for enormous losses in human life and structural facilities [1, 2]. The 1994 Northridge and 1995 Hyogoken-Nanbu earthquakes resulted in severe damage or collapse of numerous frame buildings [3, 4]. The vulnerability was particularly evident in beam-column connections and bracing joints where the plastic hinges were formed to dissipate the input energy. Therefore, careful attention should be paid to the design of such connections [5, 6]. Subsequently, researchers have focused on improving the ductile capacity in connections and mitigating structural damage induced by earthquakes. The passive control method was developed and comprehensively investigated in the past decades, which aims to dissipate the input energy using the added damping devices and prevent the damage in structural components [7–10]. Passive devices are widely used to enhance seismic performance and reduce the dynamic response of both new and retrofit buildings. They offer advantages such as ease of construction, cost-effectiveness, low maintenance requirements, and no external power requirements [11–13].

Various different types of energy dissipation devices have been proposed for passive control of structures, such as metallic dampers [14, 15], friction dampers [16, 17], and viscoelastic dampers [18, 19]. Metallic dampers hold an important position due to their stable hysteretic performance and temperature stability. Moreover, metallic dampers primarily provide additional damping and stiffness to the primary structural system. Metallic dampers were originally proposed by Kelly et al. [20] and further developed, including X-added damping and stiffness (XADAS) damper [21], triangular-added damping and stiffness (TADAS) damper [22], U-shaped steel damper [23], S-shaped steel plate damper [24], slit steel damper (SSD) [25], shear panel damper [26], buckling restrained brace

(BRB) [27], and comb-teeth damper (CTD) [28]. Ahmadi and Jamkhaneh [29, 30] applied metallic yielding damper and friction damper to steel frame on soft soil and carried out numerical analysis on these models. The results showed that both metallic damper and friction damper can effectively reduce the seismic response of the structure. The metallic dampers mentioned above would dissipate energy only if the two ends of the component experience displacement and sometimes such displacement should be large enough to cause these dampers yield. Additionally, the metallic dampers mentioned above require a significant space for installation since they usually connect to structural systems with the help of additional brace components.

It is widely accepted that the beam-column connection failures in frame structures would lead to structural collapse. To this end, innovative metallic dampers have been proposed. Garmeh et al. [31] conducted parametric studies on a rotational yielding damper and found that increasing the equivalent diameter and number of hourglass steel pins enhances its energy dissipation capacity. However, this type of damper requires steel braces to integrate with the structure, resulting in excessive occupation of building space. Khalili et al. [32] presented a damper for beam-column steel connections, which achieves energy dissipation through the flexural deformation of hourglass steel pins. Nevertheless, it is difficult to be replaced in the aftermath of earthquakes. Additionally, Dai et al. [33] investigated a fan-shaped shear damper used in the mortise-tenon joints of wooden structures, which enhances the energy dissipation capacity of the joint and effectively controls joint tenon pullout problem. Li et al. [34] proposed a rotation-amplified rubber viscoelastic damper which dissipates energy through the relative rotational deformation in the beam-column joints. However, this damper primarily relies on the viscoelastic material for energy dissipation, which offers limited stiffness and energy dissipation capacity. In addition, Ye et al. [35] introduced a lever-type lead viscoelastic damper installing at the beam-column joints. Again, the aforementioned dampers would require complete replacement after subjected to a high-intensity earthquake, resulting in significant time costs and economic losses.

The rotation-based metallic damper (RMD) proposed in this study is a type of metallic damper that also experiences a certain degree of displacement before yielding, and primarily designed for industrial buildings [36, 37]. Unlike common residential buildings, industrial buildings have stringent operational requirements, and added damping systems are not allowed to interfere with the normal operational process. In other words, damping systems which incorporate damper devices and additional braces for connecting the structural system are not friendly to industrial buildings since they would occupy significant spaces. In contrast, the RMD offers advantages of such as convenient installation and configuration independence without the need for additional braces. The study begins with a comprehensive description of the complete structure and working mechanism of the RMD. Subsequently, a series of quasistatic tests are conducted on 12 specimens to evaluate their mechanical performance and identify failure modes. Comparative analysis is performed to assess the global hysteretic responses among the specimens. Additionally, detailed analysis is carried out to evaluate the energy dissipation capacity, strength, and stiffness considering various parameters. Based on the experimental results, the influence of these parameters on the mechanical performance of the RMD is discussed. Finally, finite element (FE) analysis is conducted to simulate the specimens and validate the experimental findings.

2. Rotation-Based Metallic Damper

A structural configuration of the RMD is shown in Figure 1, which consists of an upper connecting steel plate, a middle rotary steel plate, hyperbolic-shaped steel bars (HSBs), two edge restraint steel plates, and a bottom connecting steel plate. The upper connecting steel plate is connected to the middle rotary steel plates by K groove butt joint welding; the edge restraint steel plates and the bottom connecting steel plate are also connected by K welding. The HSBs pass through one edge restraint steel plate, the middle rotary steel plate, and the other edge restraint steel plate successively. They are then fixed between the two edge restraint steel plates using high-strength nuts. The centers of the two sector-shaped edge restraint steel plates and the sector-shaped middle rotary steel plate are all located on the intersection line of the bottom and upper connecting steel plate planes. As a result, the HSBs in the damper would experience flexural deformation to dissipate energy.

As illustrated in Figure 2, the RMD is installed at the beam-to-column connections, with two connecting steel plates fixed to the adjacent column and beam. When the structure is subjected to lateral loads, rotations occur at the beam-column connections. The column rotates by an angle θ relative to the beam, resulting in a corresponding rotation θ between one connecting steel plate and the other. Consequently, the connecting steel plates transmit forces to the HSBs, inducing them to experience deformation with a displacement $\Delta_D = \theta \times R_D$. This forceful action enables the HSBs to undergo plastic deformation. In the most extreme case, all HSB elements achieve yielding, and based on such a scenario, the strength of the damper plates and bolts can be determined using the force-controlled design concept. Furthermore, by adjusting the dimensions and quantity of HSBs, the RMD can be customized to have varying levels of energy dissipation capacities and stiffness according to the specific demands of the structures. The notations for indicating the geometry of an RMD component are illustrated in Figure 3.

The RMD is designed to exhibit the following characteristics: (1) The RMD ensures a well-defined and reliable pathway for transferring lateral loads. (2) The integration of HSBs in the RMD design results in a smooth cross section, eliminating stress concentration phenomena and enabling reliable fixed-point yield functionality. (3) The RMD's seismic performance can be customized by adjusting the number and dimensions of the HSBs to meet specific requirements, thus satisfying different energy dissipation demands. (4) The RMD can function independently without requiring additional components such as braces, simplifying

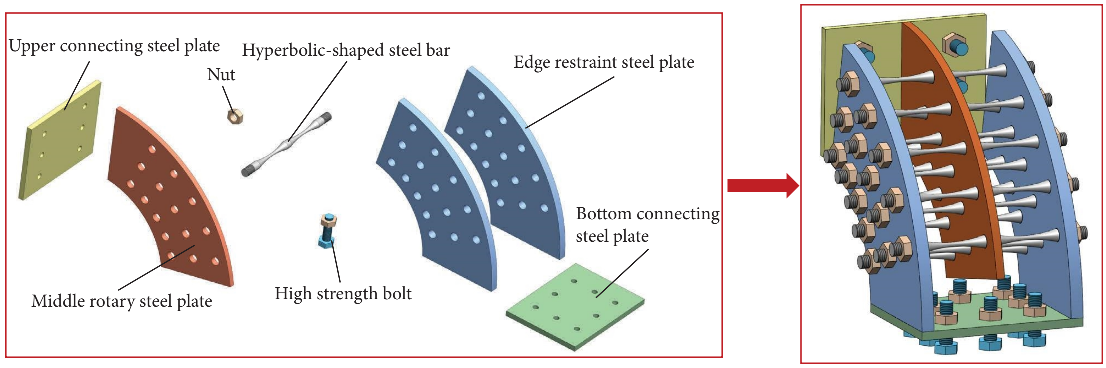

Figure 1: Three-dimensional diagram of the proposed RMD. (a) Components. (b) Assembly.

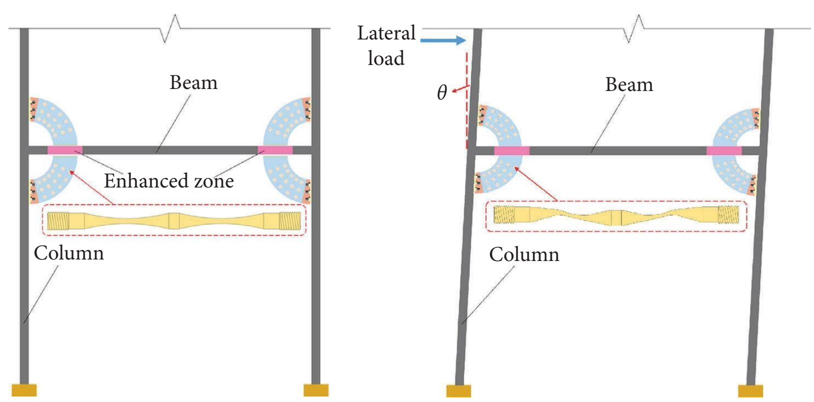

Figure 2: Diagram of operational principle of the RMD. (a) Predeformation. (b) Postdeformation.

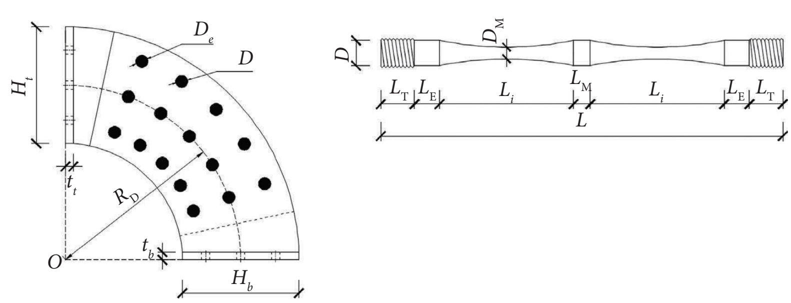

Figure 3: Dimensions of RMD components. (a) Connecting plate. (b) HSB.

installation and integration into diverse building systems. (5) After an earthquake, the RMD can be conveniently repaired or replaced, thereby promoting efficient post-earthquake functional recovery.

3. Experimental Setup and Procedure

Twelve RMD specimens were tested using predetermined protocols to examine their hysteretic behavior. This section provides a detailed description of the experimental setup and procedure.

3.1. Specimen Description. The primary objective of the experimental study is to validate the cyclic performance of the RMD, with particular emphasis on identifying failure modes and evaluating stiffness, strength, and energy dissipation capacity. Several parameters were taken into account for the RMD specimens to investigate their impact on the hysteretic behavior. Every RMD specimen was assigned a specific reference index for simplicity of illustration in the following analysis. This index comprises the first letter of the damper, the quantity of HSBs, and the diameter of HSBs D_M and concludes with R_D of the RMD, as listed in Table 1.

Considering the characteristics of the RMD and the experimental constraints, the following parameters were selected as variables for the specimens: (1) the number of the HSBs, denoted as n; (2) the length from the center of the HSBs to the center of rotation, R_D; (3) the waist diameter of the HSBs, D_M. These parameters were chosen based on similar previous studies [31, 38], as they significantly affect the energy dissipation capacity of the RMD.

3.2. Material Properties. The HSBs in the RMD were made of Q235 steel with the expected yielding strength of 235 MPa, while the remaining plate components were made of Q345 steel material. To determine the actual mechanical properties of these two steel materials and consider the configuration of the RMD components, material tests were conducted using specimens and the test setup as shown in Figure 4. The steel material properties were obtained using the same materials as those used in the RMD specimens and are summarized in Table 2.

3.3. Test Setup. Figure 5 shows the test setup, which includes a reaction wall, a horizontal hydraulic actuator, a clamp, an L-shaped linkage mechanism (consisting of a steel beam, steel column, ear steel plates, and pin shaft), a compression beam, and an RMD specimen. As shown in Figure 5(c), the specimens were installed at the beam-column joint. The beam and column have an H-shaped wide flange cross section. This joint was specifically designed, with the column hinged to the beam using a pin shaft, ensuring that the resulting hysteretic curves are not affected by inelastic behaviors of the beam and column. The ear plates were welded to both the column and beam, and additional stiffeners were placed at required locations. The specimens were secured to the beam and column using M20 high-strength bolts.

One end of the horizontal hydraulic actuator was hinged to the reaction wall, while the other end was connected to the steel column using the clamp and anchor. To ensure the stability of the entire setup, the steel beam was connected to the strong floor using a compression beam and anchor bolts. It should be noted that the steel beam is constrained, while the steel column can rotate at the pin connection, which approximates the working condition of the RMD in a frame structure under earthquake loadings. Cyclic displacement-controlled loading was applied to the top end of the steel column by the horizontal hydraulic actuator. During the test loading, the center line of the hydraulic actuator, the axis of the force transfer rod, and the center line of the clamp are aligned to ensure that the loading control generates only horizontal displacement. The actuator applies a low-cycle reciprocating load to drive the loading control in forward and backward reciprocating movements in the horizontal direction.

3.4. Loading Protocol. The quasistatic loading protocol for the twelve RMD specimens includes two stages in accordance with FEMA 461 [39] and Figure 6. In the first stage, the initial displacement amplitude was set to 1 mm, with a subsequent increment of 1 mm for each loading amplitude. One loading cycle was conducted at each loading amplitude of 1 mm to 5 mm. Afterward, when the displacement amplitude reached 10 mm, the increment was increased to 5 mm, and each amplitude level underwent three cycles. After each loading stage, the RMD was inspected for any alterations before proceeding to the subsequent loading stage. The maximum applied displacement load, irrespective of damper damage, was set to 30 mm (equivalent to an interstory drift of 0.025). Specimen D-15-10-450 underwent additional displacement up to 35 mm, and subsequently up to 40 mm to 110 mm, to further examine damaging phenomena and failure modes.

3.5. Measurements Deployment. In the experiments, the quantities of the loading force, actual displacement of the actuator, and the rotational deformation of the RMD specimens need to be measured. Three linear variable displacement transducers (LVDTs), labeled as D_1, D_2, and D_3, were used to measure the displacement at different positions on the specimens during the loading process (Figure 7(a)). The D_1 was set to measure the displacement of the bottom steel beam, D_2 was positioned to measure the vertical displacement of the upper connecting steel plate of the RMD specimens, and D_3 was arranged to measure the horizontal displacement of the actuator. The force sensor embedded in the actuator was used to measure the force. The actual displacement of the actuator is determined as the difference of the displacements measured by D_1 and D_3, which were oriented horizontally and paralleled to the actuator. The flexural moment, denoted as M, of the RMD specimens can be calculated according to (1), and the rotational deformation, represented as θ, can be determined by (2), as follows:

$$M = FH, \tag{1}$$

$$\theta = (D_3 - D_1)/H, \tag{2}$$

where F is the loading force applied by the actuator, H is the height between the loading point and the center of the pin shaft, and D_3 and D_1 are the displacement measured by the D_3 and D_1, respectively.

As the HSBs are the main energy dissipation components of the RMD, strain gauges were affixed to the surfaces of the HSBs to monitor the stress state at these critical positions, as displayed in Figure 7(b). The red line in the figure represents the placement of the strain gauges. Uniaxial strain gauges were placed perpendicular to R_{D} of the RMD to monitor their local inelastic behavior.

4. Test Results and Discussion

4.1. Test Phenomena and Failure Modes. The observed test phenomena and failure modes of the specimen D-15-10-450 are depicted in Figure 8. To facilitate the description of test observations, each reserved hole of the specimen is labeled with a number, as shown in Figure 8(a). Figure 8(b) shows the initial state of the specimen. When the displacement

Table 1: Dimensions of the specimens.

Specimen ID	H_t (mm)	t_t (mm)	H_b (mm)	t_b (mm)	D_e (mm)	D (mm)	D_M (mm)	L (mm)	L_T (mm)	L_E (mm)	L_i (mm)	L_M (mm)	n	R_D (mm)
D-1-10-450	300	20	300	20	32	30	10	480	40	30	160	20	1	450
D-3-10-450	300	20	300	20	32	30	10	480	40	30	160	20	3	450
D-6-10-450	300	20	300	20	32	30	10	480	40	30	160	20	6	450
D-9-10-450	300	20	300	20	32	30	10	480	40	30	160	20	9	450
D-12-10-450	300	20	300	20	32	30	10	480	40	30	160	20	12	450
D-9-6-450	300	20	300	20	32	30	6	480	40	30	160	20	9	450
D-9-14-450	300	20	300	20	32	30	14	480	40	30	160	20	9	450
D-9-18-450	300	20	300	20	32	30	18	480	40	30	160	20	9	450
D-3-10-352	300	20	300	20	32	30	10	480	40	30	160	20	3	352
D-3-10-450	300	20	300	20	32	30	10	480	40	30	160	20	3	450
D-3-10-548	300	20	300	20	32	30	10	480	40	30	160	20	3	548
D-15-10-450	300	20	300	20	32	30	10	480	40	30	160	20	15	450

Table 2: Material property test results.

Material	Thickness/diameter (mm)	Young's modulus (GPa)	Yield stress (MPa)	Ultimate stress (MPa)	Elongation (%)
Q345	10	208	348.47	500.37	24
Q235	8	207	235.13	417.03	27

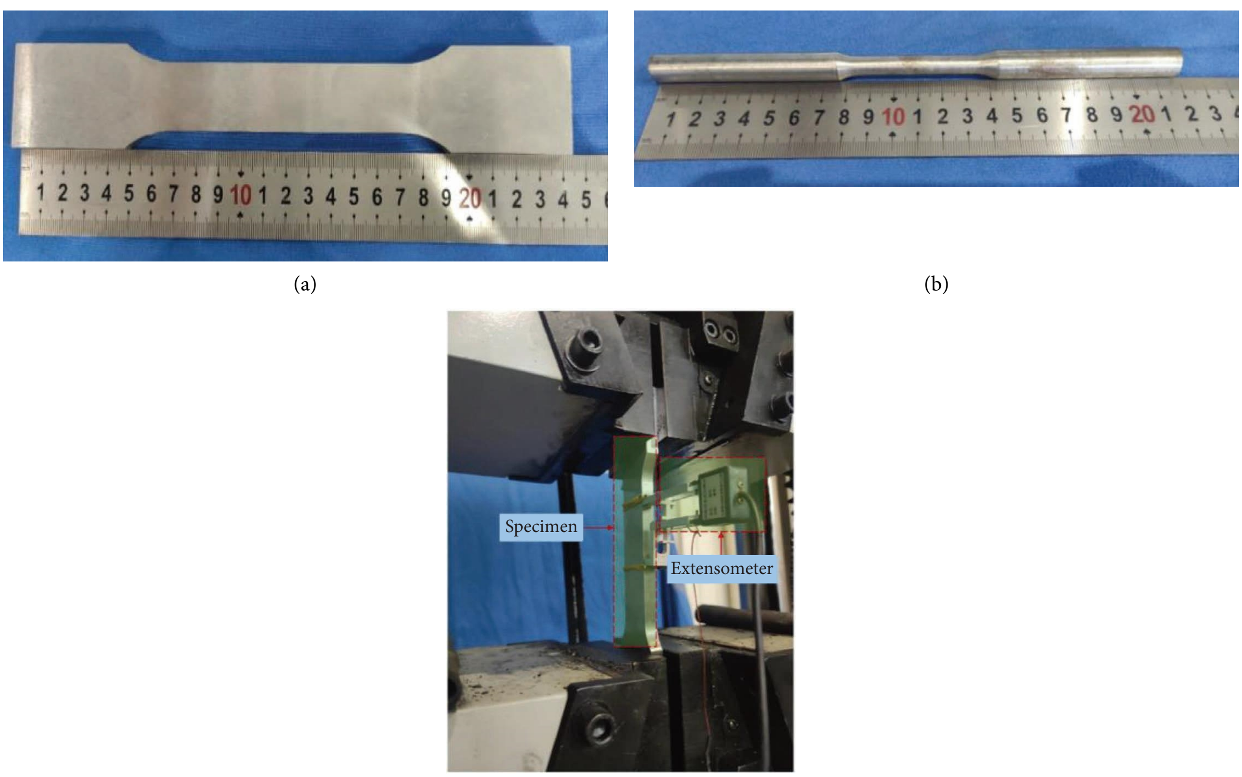

(a) (b) (c)

Figure 4: Steel material property test. (a) Q345 steel. (b) Q235 steel. (c) Test setup.

loading reached 30 mm, the HSBs exhibited significant deformation, as illustrated in Figure 8(c). Plastic deformation was observed at a displacement loading of 55 mm, as shown in Figure 8(d). When the displacement loading was −80 mm, HSBs #5 and #10 fractured, as shown in Figure 8(e). In the first cycle, at a displacement of −85 mm, HSB #2 fractured, as shown in Figure 8(f). In the second cycle, with the displacement loading of 85 mm, HSB #4 fractured, as shown in Figure 8(g). Subsequently, in the second cycle at a displacement of −85 mm, HSB #3 fractured, as shown in Figure 8(h). Moving on to the third cycle, HSBs #1 and #6 fractured, as shown in Figure 8(h), at

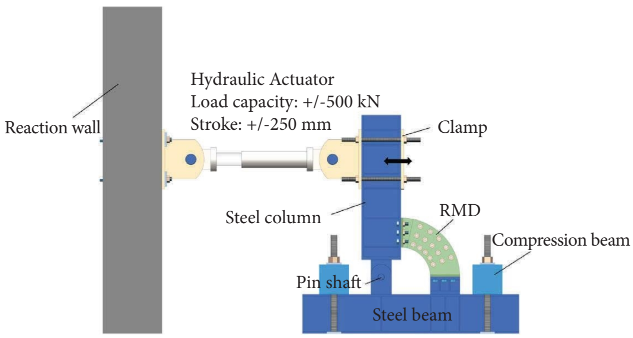

(a)

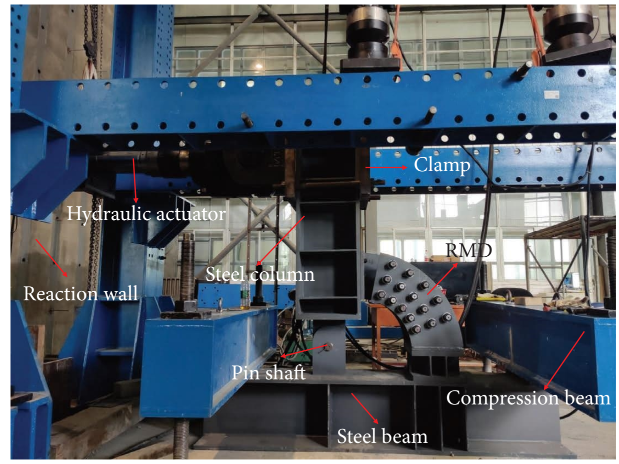

(b)

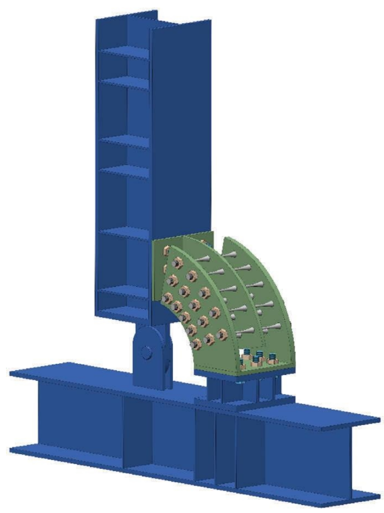

(c)

FIGURE 5: Experimental setup. (a) Schematic of test setup. (b) Picture of test setup. (c) Specimen installation.

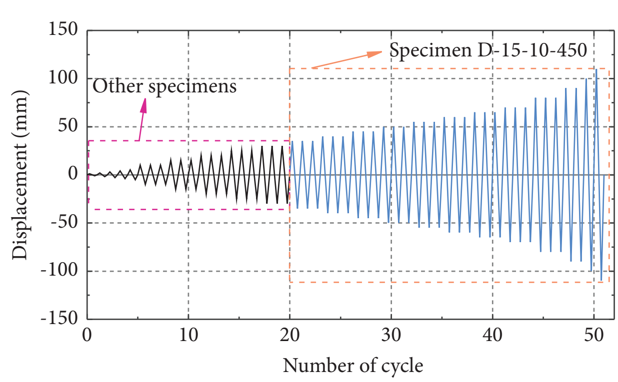

FIGURE 6: Loading protocol.

a displacement of 85 mm, while HSB #9 fractured (Figure 8(h)) at a displacement loading of −85 mm. Furthermore, at a displacement loading of 90 mm, HSB #15 fractured, as depicted in Figure 8(i), and at displacement loading of 100 mm, HSBs #7 and #8 fractured, as shown in Figure 8(j). Finally, at a displacement loading of −110 mm, HSBs #11 and #12 fractured successively, as illustrated in Figure 8(k).

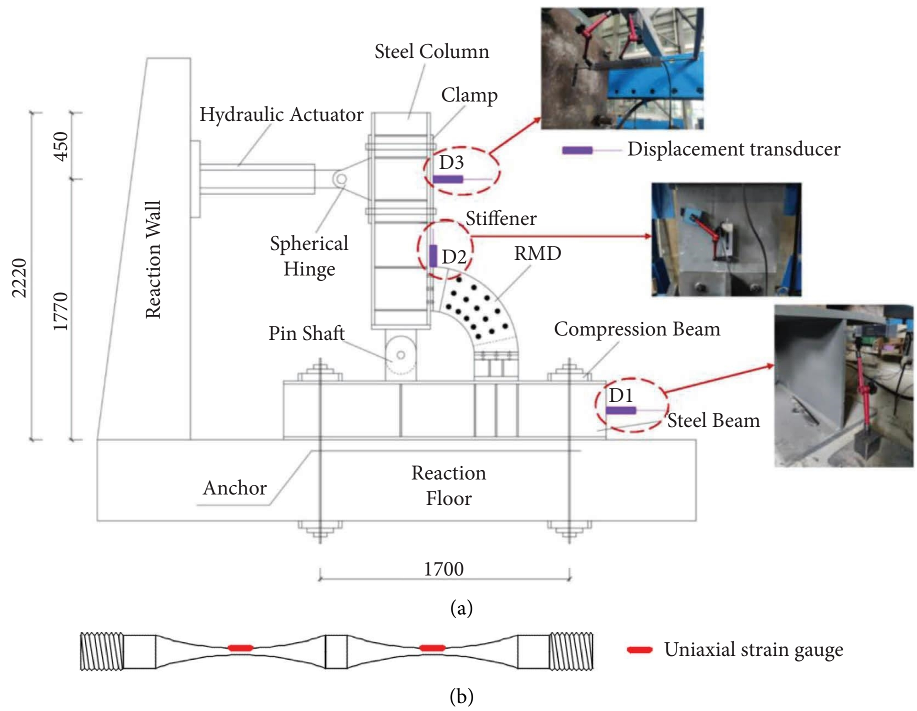

FIGURE 7: Layout of displacement transducers and strain gauges (unit: mm). (a) Displacement transducers. (b) Strain gauges.

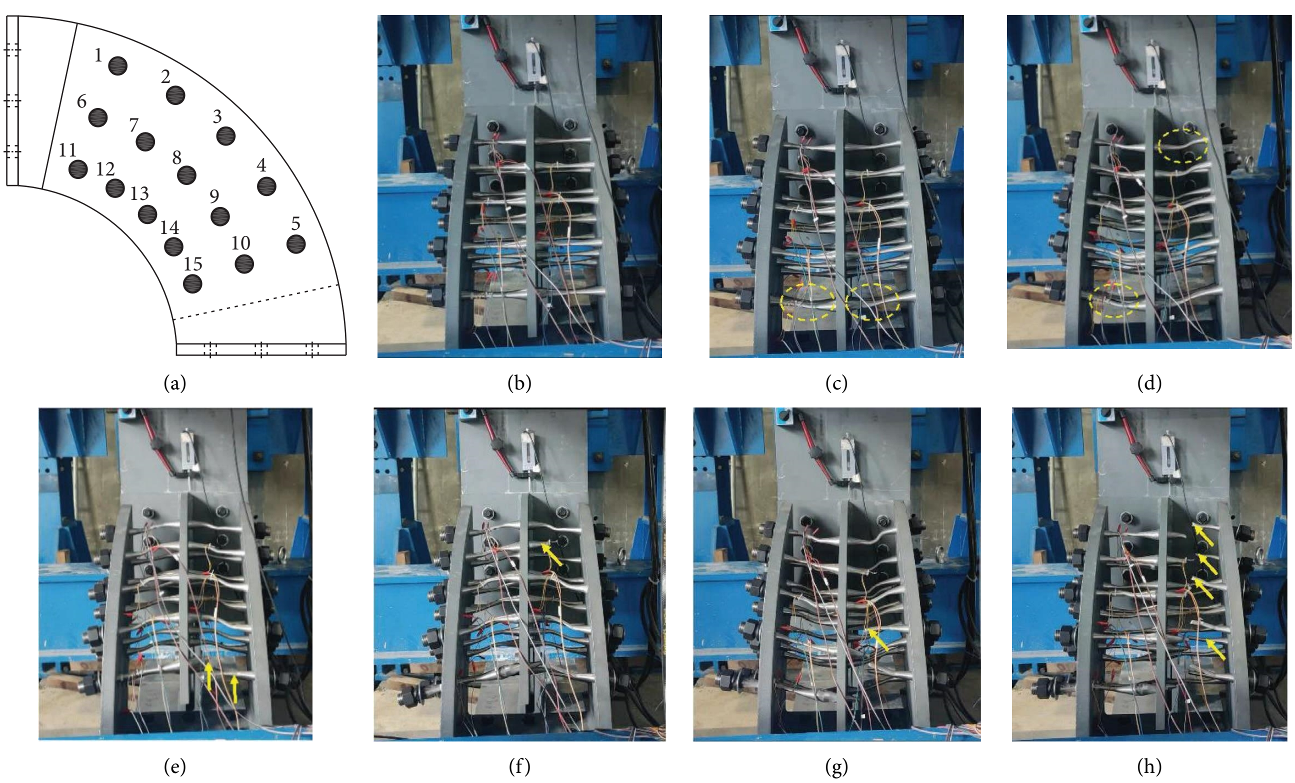

FIGURE 8: Continued.

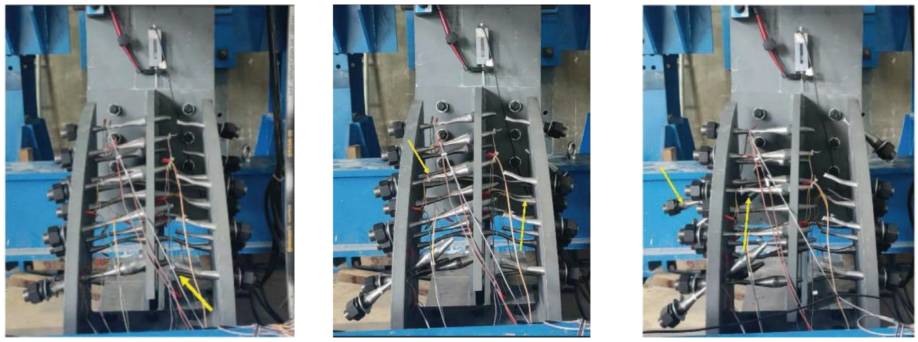

(i) (j) (k)

Figure 8: Test phenomena and failure mode of specimen D-15-10-450. (a) Label of the HSBs. (b) Initial state. (c) Obvious deformation. (d) Plastic deformation. (e) No. 5, 10 fractured. (f) No. 2 fractured. (g) No. 4 fractured. (h) No. 3, 1, 6, 9 fractured. (i) No. 15 fractured. (j) No. 7, 8 fractured. (k) No. 11, 12 fractured.

4.2. Parametric Test Results

4.2.1. Effect of the Number of HSBs. This section primarily evaluates the influence of the number of HSBs (i.e., n) on the behavior of the RMD specimens. Figure 9 compares the hysteresis curves of specimens D-1-10-450, D-3-10-450, D-6-10-450, D-9-10-450, and D-12-10-450. It can be observed that all five specimens exhibit stable hysteretic performance, with a slight pinch phenomenon occurring in the middle of the hysteresis curves. This pinch phenomenon is caused by the gaps between the HSBs and adjacent steel plates. The contact delay due to the gaps caused the pinching phenomenon observed in the hysteresis curves of the specimens and similar findings were noted in prior studies like Li et al. [40]. During the test loading process, the loosening of the nut can also cause pinching of the hysteresis curve. Shen et al. [41] explained and verified this phenomenon by comparing the hysteresis curves of the two different connections with bolted web links and welded end-plate links. It was found that the hysteresis curves of the bolted links showed a more obvious pinch phenomenon, while the hysteresis curve of the welded links was more saturated. Furthermore, to facilitate installation, the diameter of the reserved holes on the edge restraint steel plates and the middle rotary steel plate is slightly larger than the diameter of the HSBs, thereby amplifying the pinch phenomenon.

According to the observed results, it was found that the ultimate strength increase with the increase of number of HSBs. For example, by increasing the number of HSBs from 1 to 3, the ultimate strength increased by approximately 71.35%. Similarly, increasing the number of HSBs from 3 to 6 resulted in an ultimate strength increase of about 26.05%, and increasing the number of HSBs from 9 to 12 led to an ultimate strength increase of approximately 46.51%. Furthermore, the strength of specimens with a higher number of HSBs exhibited a larger rate of strength increase. Additionally, specimens with a higher number of HSBs exhibited smaller residual deformation.

To further investigate the energy dissipation capacity of the RMD specimens, the equivalent damping ratio ζ_{eq} was defined by the following equation.

$$\zeta_{\mathrm{eq}} = \frac{1}{2\pi} \cdot \frac{S_{(ABC+CDA)}}{S_{(OBE+ODF)}}, \tag{3}$$

where $S_{(ABC+CDA)}$ is the area of the hysteresis loop $ABCD$ and $S_{(OBE+ODF)}$ is the sum of the areas of triangles OBE and ODF, as shown in Figure 10.

Figure 11 presents the curves of the equivalent damping ratio ζ_{eq} (Figure 11(a)) and the amounts of dissipated energy (Figure 11(b)) for the RMD specimens during the first cycle of loading at each displacement level. It can be observed that ζ_{eq} decreases as the number of HSBs increases. This implies that the specimens with a lower number of HSBs exhibit higher values of ζ_{eq}. For instance, when the number of HSB is 1, the specimen RMD shows an ζ_{eq} of approximately 43.76% at a displacement of 10 mm during the first cycle. The full section yielding characteristic allows for uniform distribution of yielding across the HSBs, resulting in a higher ζ_{eq}. Conversely, the amounts of dissipated energy increase as the number of the HSBs increases. For instance, at a displacement of 30 mm during the first cycle, specimen D-3-10-450 dissipates approximately 29.86% more energy compared to specimen D-1-10-450. When the number of HSBs increases from 3 to 6, the amounts of dissipated energy increase by about 20.25%. Table 3 displays the total energy dissipation of specimens with varying number of HSBs. As observed in Figure 11(b), specimens with higher number exhibit increased energy dissipation capacity.

Figure 12 illustrates the influence of the number of HSBs on the equivalent stiffness, K and determined by (4), as well as the strength degradation of the specimens, λ_n, as given in (5):

$$K_i = \frac{\left|+P_{i\,\max}\right| + \left|-P_{i\,\max}\right|}{\left|+\Delta_{i\,\max}\right| + \left|-\Delta_{i\,\max}\right|}, \tag{4}$$

$$\lambda_n = \frac{F_n}{F_1}, \tag{5}$$

where $+P_{i\,\max}$ and $-P_{i\,\max}$ are the positive and negative loads of the i^{th} cycle, respectively, $+\Delta_{i\,\max}$ and $-\Delta_{i\,\max}$ are the corresponding displacements, F_n and F_1 are the peak loads of the last loading cycle and first loading cycle under the

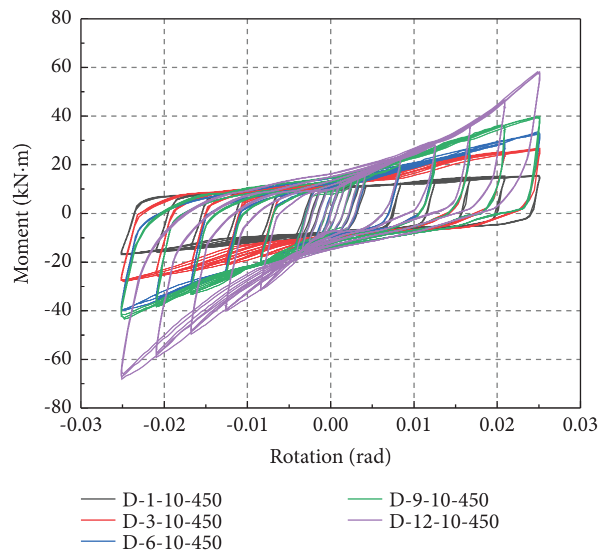

Figure 9: Hysteresis curves.

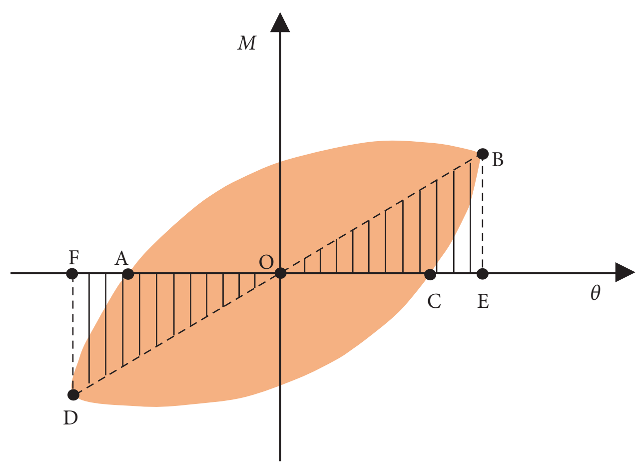

Figure 10: Solution of ζ_{eq}.

same loading amplitude, and λ_3 is used to represent the strength degradation in the subsequent analysis as each loading level underwent three cycles.

It is evident that an increase in the number of HSBs results in a higher equivalent stiffness (Figure 12(a)). For instance, when the number increases from 3 to 6, the equivalent stiffness increases by approximately 35.36% during the first cycle at a displacement of 30 mm. Moreover, the strength of the RMD specimens does not exhibit significant attenuation with repeated and increased displacement loading (Figure 12(b)). Therefore, the number of HSBs significantly affects the energy dissipation capacity of the RMD specimens.

4.2.2. Effect of R_D of RMD. The hysteresis curves of RMD specimens with various R_D are compared in Figure 13(a). It is evident that R_D significantly affects the energy dissipation capability and strength of the RMD specimens. Furthermore, the ultimate strength of the specimens increases with an increase in R_D. For instance, the ultimate strength of specimen D-3-10-548 is approximately 21.46% and 39.34% higher than that of specimens D-3-10-450 and D-3-10-352, respectively. Additionally, the strength of the specimens with a large R_D increases rapidly and the residual deformation is small. Figure 13(b) shows the curves of ζ_{eq} for specimens with various R_D. As shown in Figure 13(b), specimens with smaller R_D exhibit higher ζ_{eq}. Conversely, Figure 13(c) shows that the amounts of dissipated energy increases as R_D increases. For instance, increasing R_D from 352 mm to 450 mm and from 450 mm to 548 mm results in an approximately 5.54% and 11.65% increase in the dissipated energy, respectively, at a displacement loading of 25 mm.

Table 4 lists the amounts of total dissipated energy for specimens with various R_D. The data clearly demonstrate that increasing R_D leads to higher amounts of dissipated energy, indicating an enhanced energy dissipation capability.

Figure 14(a) illustrates the influence of R_D on the equivalent stiffness of the RMD specimens. The results

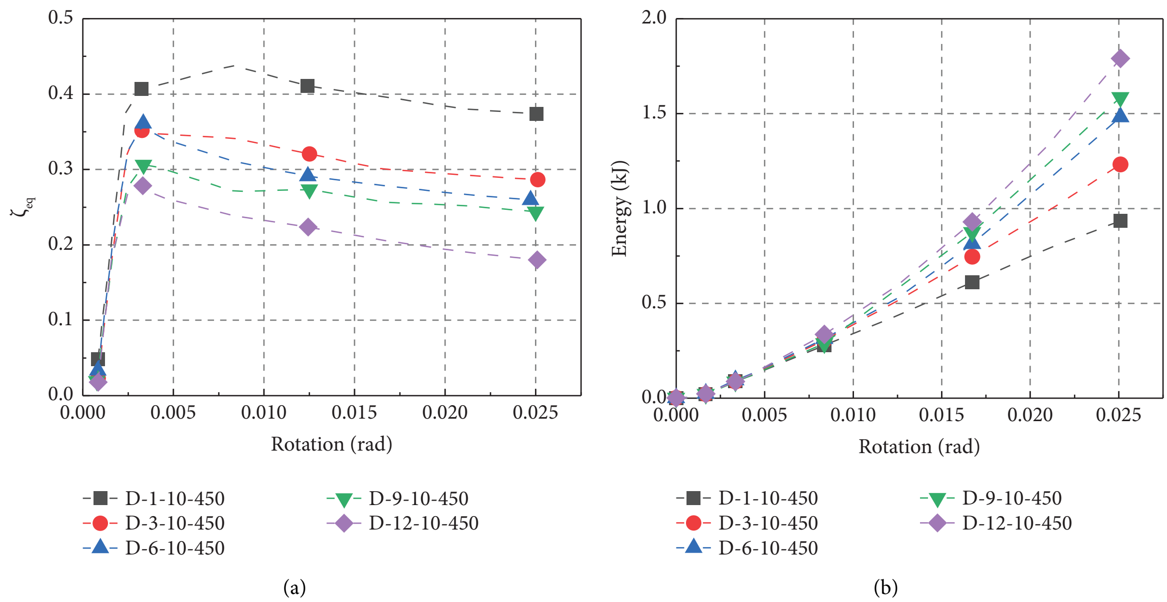

Figure 11: Energy dissipation capacity of specimens with various number of HSBs. (a) Equivalent damping ratio ζ_{eq}. (b) Dissipated energy during first cycle.

Table 3: Total dissipated energy of specimens with various number of HSBs.

Specimens	Energy (J)
D-1-10-450	9342.2
D-3-10-450	11442.1
D-6-10-450	13054.5
D-9-10-450	13945.6
D-12-10-450	14930.4

demonstrate that the equivalent stiffness increases with an increase in R_D. For instance, at a first cycle displacement level of 15 mm, specimen D-3-10-450 exhibits a 15.28% higher equivalent stiffness compared to specimen D-3-10-352. Furthermore, increasing R_D from 450 mm to 548 mm leads to an approximately 29.26% increase in the equivalent stiffness. In Figure 14(b), the strength degradation coefficient values are depicted, ranging from 0.95 to 1.03. These values indicate that the strength of the specimens with various R_D does not significantly decrease under cyclic displacement loading.

4.2.3. Effect of the HSBs with Various D_M. Figure 15(a) illustrates the hysteresis curves of specimens with various D_M. The results clearly indicate that D_M of the HSBs significantly impact the energy dissipation capability and strength of the RMD specimens. For example, an increase in D_M from 6 mm to 10 mm results in a substantial 17.70% increase in the ultimate strength. Furthermore, the ultimate strength of specimen D-9-18-450 is enhanced by 26.05% compared to specimen D-9-14-450. Additionally, with the increase of D_M, the growth rate of the strength of the specimen gradually increase. The specimens with larger D_M have larger unloading stiffness and smaller residual deformation.

Figure 15(b) shows the effect of D_M on the ζ_{eq} of the RMD specimens. It can be observed that ζ_{eq} decreases as D_M increases. Conversely, Figure 15(c) demonstrates that the amounts of dissipated energy exhibit a higher rate of increase with higher D_M values. For example, at a first cycle displacement loading level of 30 mm, specimen D-9-18-450 dissipates approximately 33.32% more energy compared to specimen D-9-14-450. Additionally, there is a 38.45% increase in the amounts of dissipated energy when D_M increases from 10 mm to 14 mm.

Table 5 presents the total energy dissipation of specimens with various D_M throughout the entire testing process. It can be observed that the total amount of dissipated energy increases by 26.60% when D_M increases from 6 mm to 10 mm. This indicates that the parameter D_M has a significant influence on the energy dissipation capacity of the RMD specimens.

Figure 16 compares the equivalent stiffness curves and strength degradation coefficient curves of specimens D-9-6-450, D-9-10-450, D-9-14-450, and D-9-18-450. Figure 16(a) clearly demonstrates the impact of D_M on the equivalent stiffness of the RMD specimens. For instance, increasing D_M from 6 mm to 10 mm results in a 41.86% increase in equivalent stiffness at the first cycle of 30 mm displacement loading level. Additionally, the equivalent stiffness of the specimen D-9-18-450 is approximately 26.49% higher compared to specimen D-9-14-450. These findings indicate that changing D_M significantly affects the equivalent stiffness of the RMD specimens. Moreover, Figure 16(b) shows that specimen D-9-6-450 exhibits a phenomenon of strength reduction compared to specimens D-9-10-450, D-9-14-450, and D-9-18-450. This can be attributed to the smaller D_M of specimen D-9-6-450, which is more prone to irreversible plastic deformation under multiple cycles of the same displacement amplitude. Overall, the strength reduction

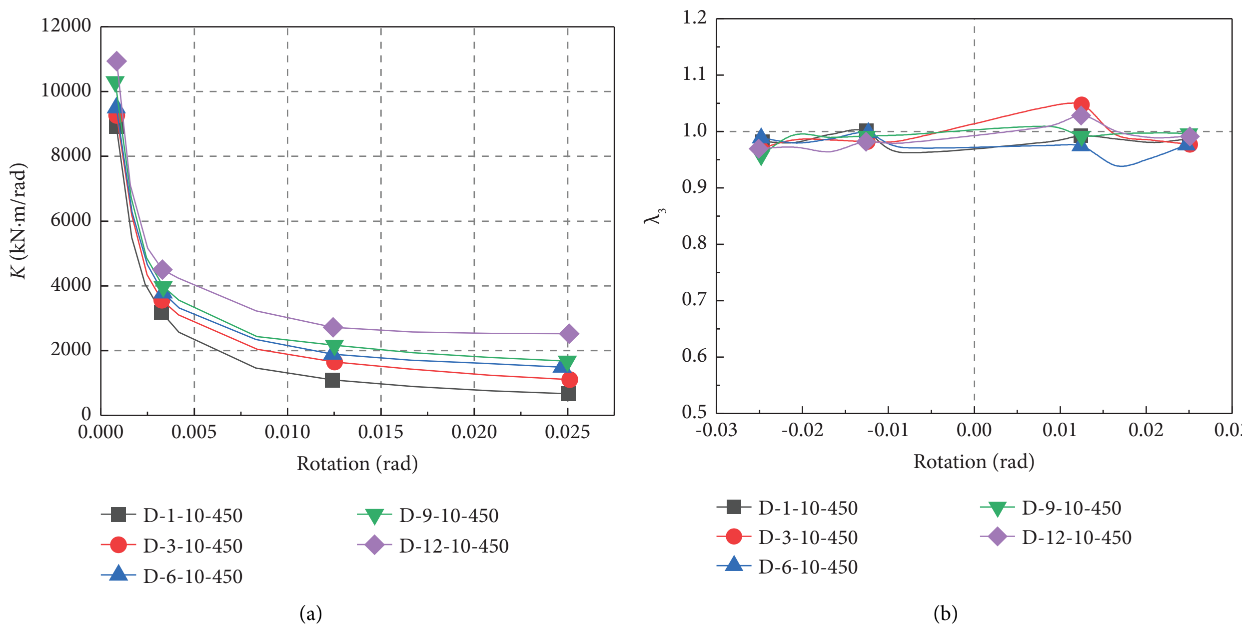

Figure 12: Stiffness and strength of specimens with various number of HSBs. (a) Equivalent stiffness. (b) Strength degradation ratio λ_3.

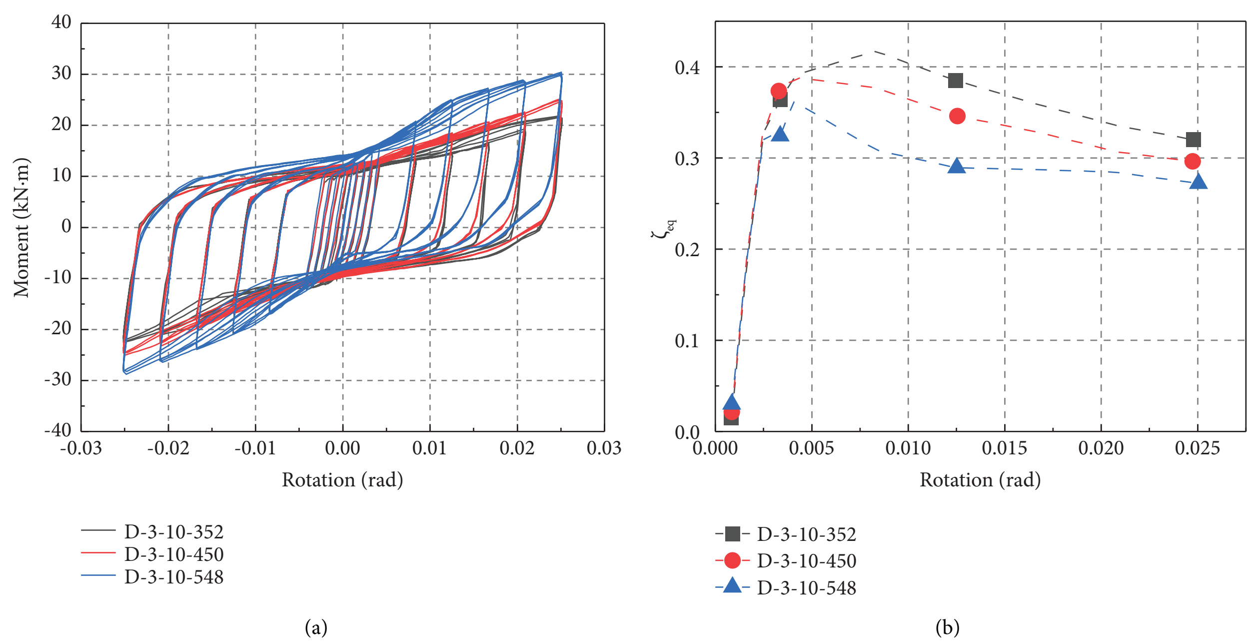

Figure 13: Continued.

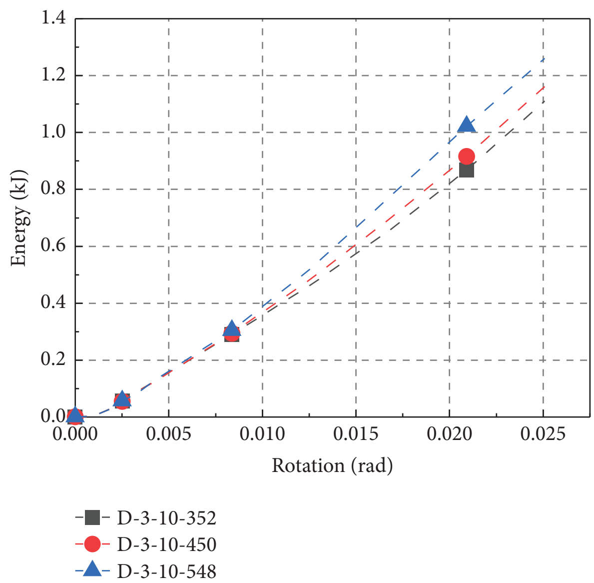

(c)

FIGURE 13: Energy dissipation capacity of specimens with various R_D. (a) Hysteresis curves. (b) Equivalent damping ratio ζ_{eq}. (c) Dissipated energy during first cycle.

TABLE 4: The total energy dissipation of specimens with various R_D.

Specimens	Energy (J)
D-3-10-352	10349.4
D-3-10-450	10784.6
D-3-10-548	11671.9

coefficient of the specimens with various D_M ranges from 0.93 to 1.05, indicating stable performance of the RMD specimens.

5. Finite Element Analysis

5.1. Finite Element Modeling. In this section, the finite element (FE) model of the RMD was established using the ABAQUS software [42]. In order to enhance computational efficiency and reduce the analysis time, the FE analysis of specimen D-3-10-352 was carried out in ABAQUS. The hysteretic responses of the RMD were verified by comparing against the experimental results.

The hinge connection between the steel column and beam was simulated using a connector with hinge properties. The cyclic loading behaviors of the HSBs were simulated using a combined hardening model, which incorporates both isotropic hardening and kinematic hardening [43, 44]. The edge restraint steel plates and the middle rotary steel plate are modeled with two-linear stress-strain relation. Furthermore, as the other components such as upper connecting steel plate and bottom connecting steel plate did not exhibit significant plastic deformation during the test, an ideal elastic model was employed to simulate their behavior. Poisson's ratio of all steel materials is set to 0.3.

Figure 17(a) shows the boundary condition setup of the FE model. The linkage mechanism, which solely provides rotational functionality without participating in energy dissipation, is constrained as rigid body. The bottom of the steel beam is fixed to prevent sliding during the loading process. Rotation loading is applied to the connector. To account for the surface interaction, a surface-to-surface contact model with friction properties is employed. A Lagrange multiplier friction coefficient of 0.3 is applied in the tangential direction, and "hard contact" is enforced in the normal direction for all contact friction applications. As the linkage mechanism does not experience deformation, the moment, rotation, and moment of the damper are solely determined by the FE model.

The C3D8R elements are used to simulate the RMD model, which refers to the eight-node hexahedron linear reduced-integration element with hourglass control. To balance the trade-off between computation time and accuracy, specific mesh sizes are employed for different components. The mesh size of the HSBs, steel plates, column, and beam was selected as 5 mm, 10 mm, 40 mm, and 110 mm, respectively. Figure 17(b) shows a visual representation of the mesh and interaction configuration.

5.2. Validations and Discussion of the Results. According to the specified test conditions, the FE model is subjected to the same loading conditions, and the results obtained from the FE analysis are compared with the experimental results to validate the accuracy of the FE model. The comparison is presented in Figures 18 and 19. Figure 18 shows that the deformation of the HSBs in the FE analysis is consistent with

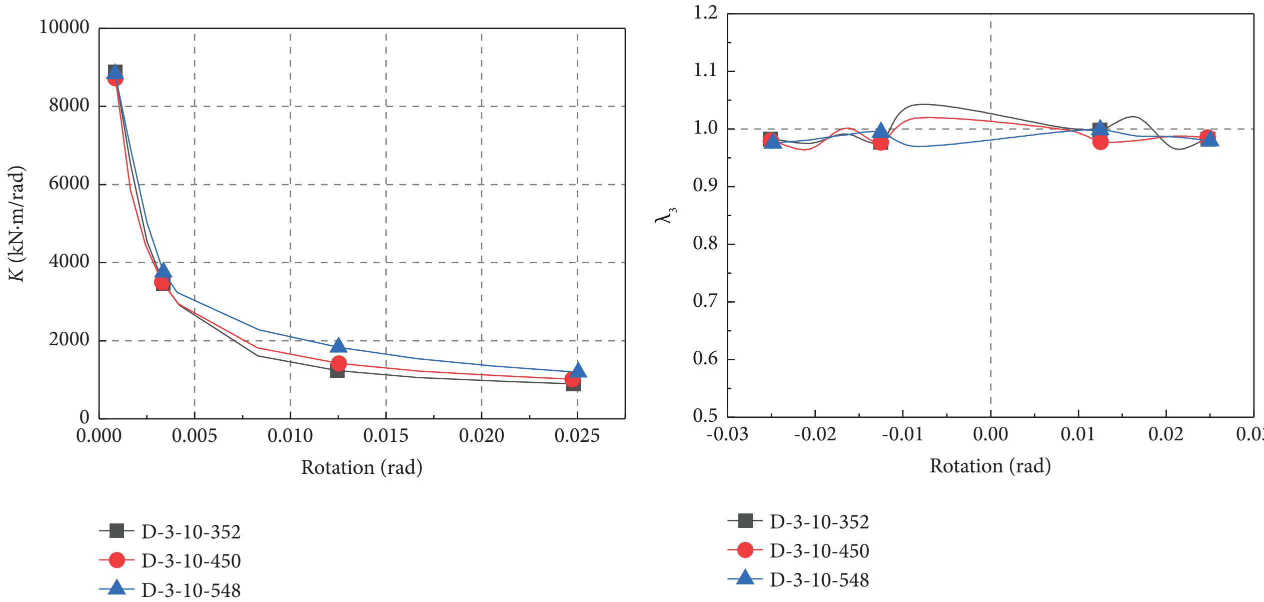

(a) (b)

FIGURE 14: Stiffness and strength of specimens with various R_D. (a) Equivalent stiffness. (b) Strength degradation ratio λ_3.

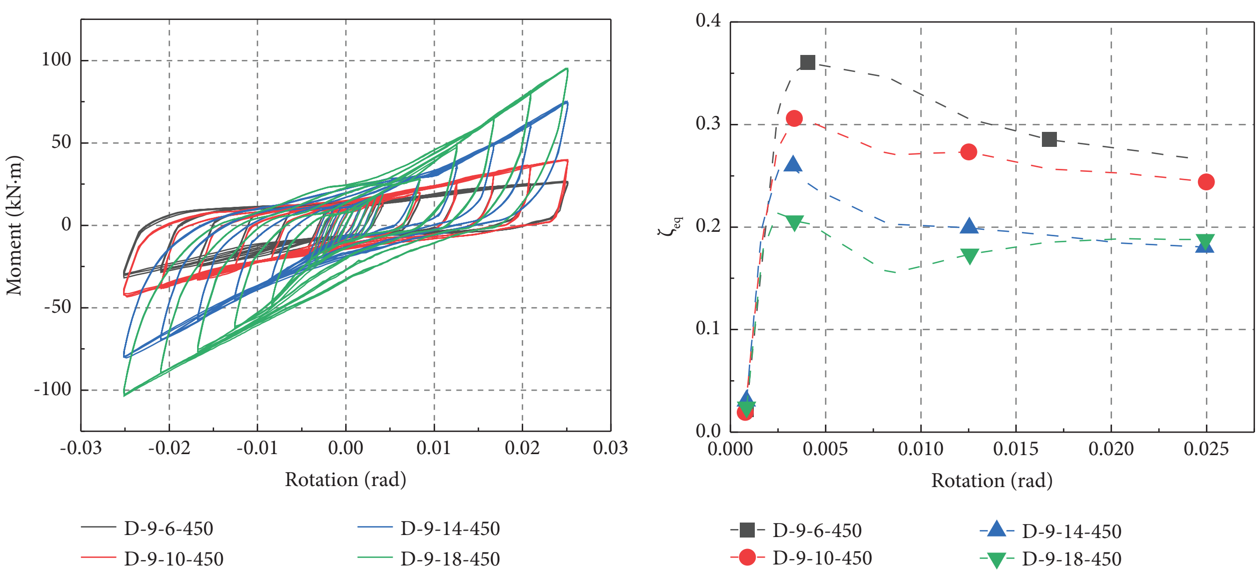

(a) (b)

FIGURE 15: Continued.

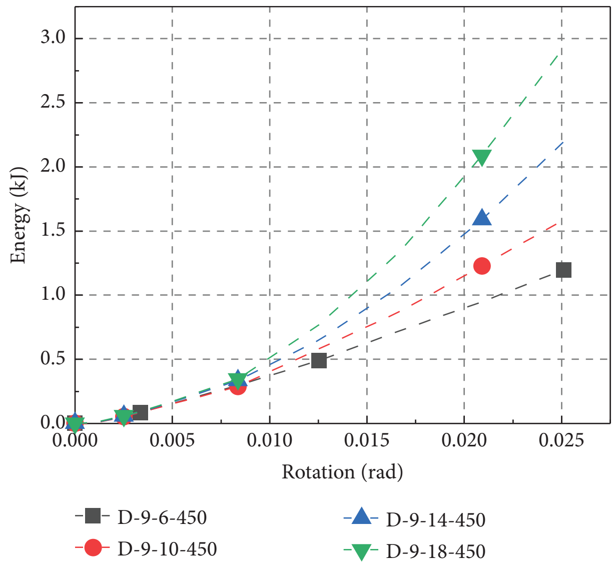

(c)

Figure 15: Energy dissipation capacity of specimens with various D_M. (a) Hysteresis curves. (b) Equivalent damping ratio ζ_{eq}. (c) Dissipated energy during first cycle.

Table 5: The total energy dissipation of specimens with various D_M.

Specimens	Energy (J)
D-9-6-450	11015.4
D-9-10-450	13945.6
D-9-14-450	17627.8
D-9-18-450	22661.5

experiment, concentrated in the middle but not at the center, and the deformation mode and high stress regions of the HSBs are identical to the specimens. Damage at the minimum diameter of the HSBs and the connection with the sector steel plate is avoided, which would cause the RMD to quit working prematurely. Figure 19 clearly demonstrates that the experiment result is close to the FE result, indicating a good agreement between the specimen and the FE model in terms of strength and stiffness. As a result, the FE model is deemed capable of accurately simulating the hysteretic behavior of the RMD and can be utilized for further analysis with confidence.

To further elucidate the energy dissipation principle of the RMD, the numerical analysis method is employed to investigate the energy dissipation process of the HSBs. Figure 20 shows the Von Mises stress distribution of the deformed HSBs. Initially, when the RMD is not suffered from external loadings, the stress of the HSBs remains at zero, depicted by the coloration blue. As the rotation reaches 0.0042, the stress of the HSBs increases and reaches the yielding strength. With gradual loading increments, the stress of the HSBs extends to both ends along the axis of the HSBs. The red area signifies the yielding area, where high stress is primarily concentrated in the preset energy dissipation region. Notably, the stress at the connecting regions between the HSBs and the connecting plates is relatively low, as is the stress at D_M of the HSBs.

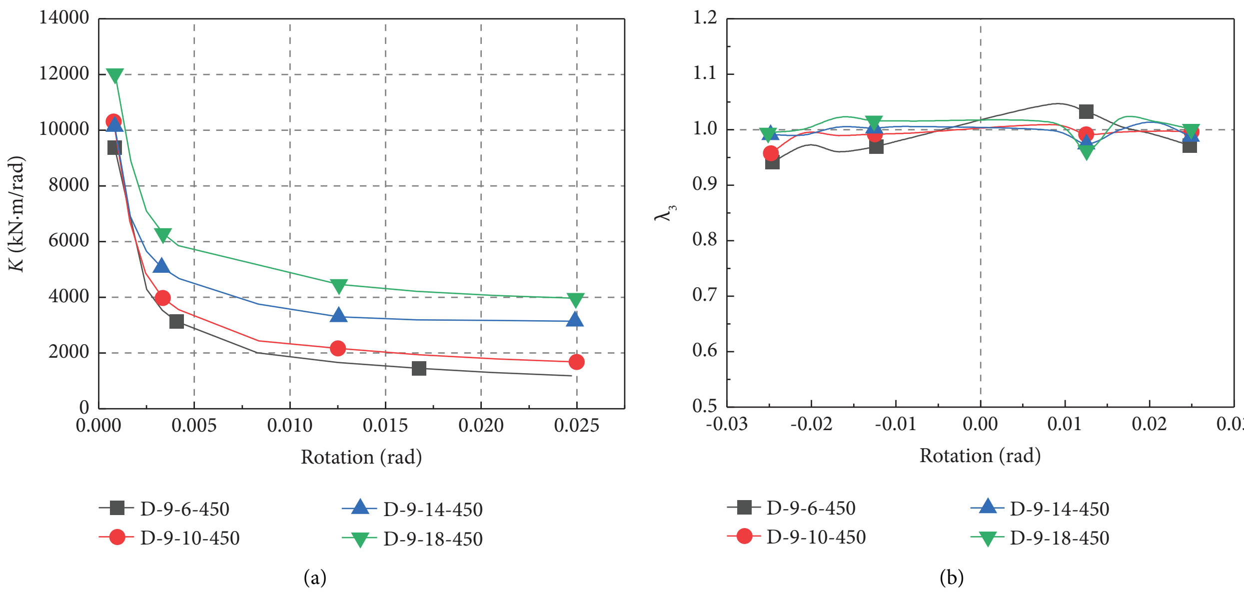

Figure 16: Stiffness and strength of specimens with various D_M. (a) Equivalent stiffness. (b) Strength degradation ratio λ_3.

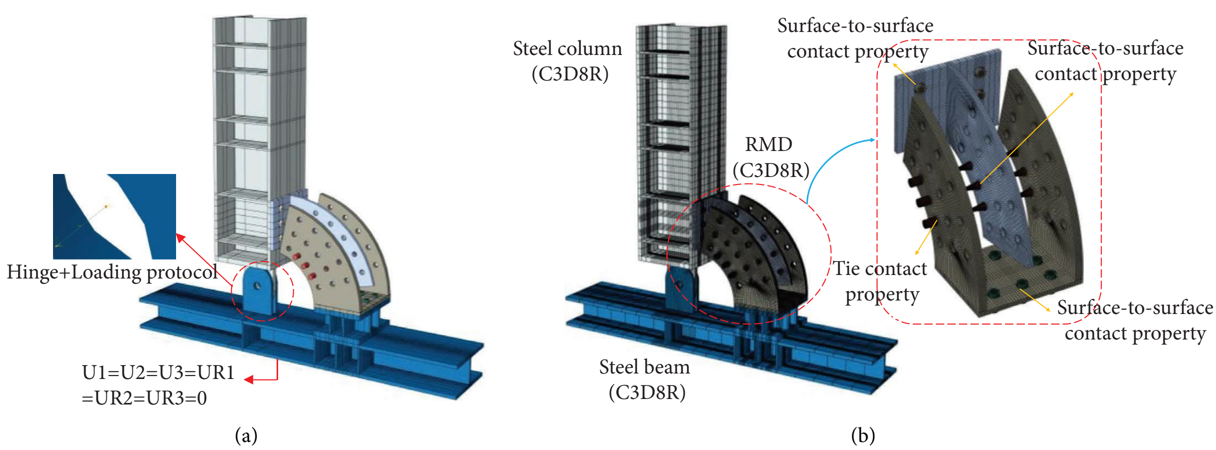

Figure 17: FE model of D-3-10-352. (a) Boundary condition. (b) Mesh and interaction on the damper.

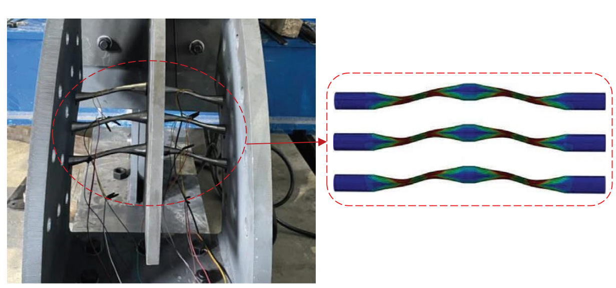

Figure 18: Comparison of experiment and FE deformation of HSBs.

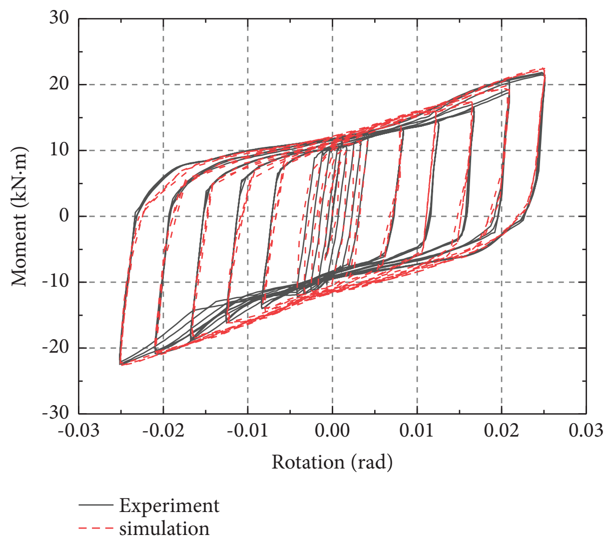

FIGURE 19: The hysteretic curves for test and simulation.

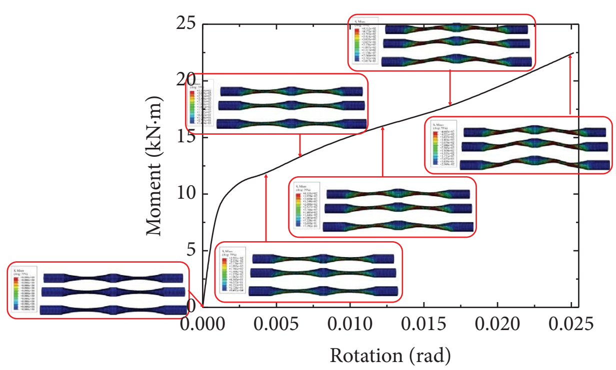

FIGURE 20: Von Mises stress distribution of deformed HSBs.

6. Conclusions and Discussion

This paper presents a novel metallic yielding damper, referred to as the rotation-based metallic damper (RMD), which exhibits stable hysteretic curve and high energy dissipation capacity. The RMD dissipates input energy through the inelastic deformation of hyperbolic-shaped steel bars (HSBs) embedded within it. To assess the mechanical properties of the RMD, twelve specimens were designed and tested under quasistatic cyclic loading. Three damper parameters, including the number of HSBs, the length from the center of the HSBs to the center of the rotation, and the waist diameter of the HSBs, were investigated. The mechanical properties, including strength, effective stiffness, and energy dissipation capacity of the specimens, were evaluated and discussed based on the experiment results. The most important findings are summarized as follows:

(1) The strength, energy dissipation capacity, and equivalent stiffness of the specimens increased with an increase in the quantity of HSBs. However, a higher number of HSBs resulted in a decrease in the equivalent damping ratio.

(2) Increasing the length from the center of the HSBs to the center of rotation of the specimen resulted in higher energy dissipation capacity, strength, and equivalent stiffness.

(3) An increase in the waist diameter of the HSBs led to higher energy dissipation capacity, strength, and equivalent stiffness of the specimen, while gradually decreasing the equivalent damping ratio. The specimens exhibited a highest equivalent damping ratio of approximately 0.45, indicating a high energy dissipation capacity.

(4) The FE model demonstrated a reasonable ability to simulate the hysteretic behavior of the RMD specimen, enabling further analysis.

In conclusion, the RMD exhibits stable hysteretic performance under cyclic loading and proves to be a suitable device for seismic strengthening or retrofitting of structures. The findings from this study contribute to a better understanding of the RMD's behavior and provide valuable insights for its practical application in seismic engineering.

One limitation of the manuscript is that the analysis focused on quasistatic cyclic loading condition, and the findings may not be directly applicable to other loading conditions. Comprehensive analytical derivations or numerical simulations would be performed in the future to explore the energy dissipation principle of the RMD in depth. Furthermore, other numerical simulations or experimental tests would be conducted to accurately identify the pinching phenomenon in the hysteresis curves and the potential influence of manufacturing tolerances or assembly variations on the performance of the RMD. Comprehensive sensitivity analysis will be conducted to assess the relative importance of every potential influential parameter on the performance of the RMD in future work. Future studies are needed to investigate the generalization of the research results. Experiments involving dynamic cyclic loading of the RMD will be conducted to investigate the low-cycle fatigue of HSBs and further enhance the understanding of the device's behaviors. Subsequently, numerical analysis at the system level will be carried out to investigate the effectiveness of the RMD in mitigating the seismic response of the structures.

To better apply the RMD to practical engineering structures, discussions on structural integrity, post-earthquake recovery, feasibility, and cost-effectiveness are necessary. Other high-performance materials with self-centering can be employed to enhance the mechanical performance and postearthquake recovery capacity of the RMD. Vulnerability analysis and seismic loss estimation of the damper-frame system will be conducted to better evaluate the feasibility and postearthquake repairability. Similarly, the discussion of the cost-effectiveness of applying RMD in actual structures will contribute to the application prospects of RMD.

Data Availability

The experimental data used to support the findings of this study are available from the corresponding author upon request.

Conflicts of Interest

The authors declare that they have no conflicts of interest.

Acknowledgments

The authors would like to acknowledge the support from the National Key Research and Development Program of China (2022YFE0113600), Science and Technology Project of Deyang City (2021BJZ002), and Dongfang Electric Wind Power Company Research Program (DEC8700CG202200279 and DEC8700CG202106045) and the Natural Science Foundation of Sichuan Province (2023NSFSC0883 and 2022NSFSC1159).

References

[1] G. L. Cole, R. P. Dhakal, and F. M. Turner, "Building pounding damage observed in the 2011 Christchurch earthquake," *Earthquake Engineering & Structural Dynamics*, vol. 41, no. 5, pp. 893–913, 2012.

[2] B. Zhao, F. Taucer, and T. Rossetto, "Field investigation on the performance of building structures during the 12 May 2008 Wenchuan earthquake in China," *Engineering Structures*, vol. 31, no. 8, pp. 1707–1723, 2009.

[3] D. K. Miller, "Lessons learned from the Northridge earthquake," *Engineering Structures*, vol. 20, no. 4-6, pp. 249–260, 1998.

[4] M. Nakashima, K. Inoue, and M. Tada, "Classification of damage to steel buildings observed in the 1995 Hyogoken-Nanbu earthquake," *Engineering Structures*, vol. 20, no. 4-6, pp. 271–281, 1998.

[5] Y. Kitagawa and H. Hiraishi, "Overview of the 1995 Hyogo-Ken Nanbu earthquake and proposals for earthquake mitigation measures," *Journal of JAEE*, vol. 4, no. 3, pp. 1–29, 2004.

[6] A. Azizinamini and S. K. Ghosh, "Steel reinforced concrete structures in 1995 Hyogoken-Nanbu earthquake," *Journal of Structural Engineering*, vol. 123, no. 8, pp. 986–992, 1997.

[7] B. Basu, O. S. Bursi, F. Casciati et al., "A European Association for the control of structures joint perspective. Recent studies in civil structural control across Europe," *Structural Control and Health Monitoring*, vol. 21, no. 12, pp. 1414–1436, 2014.

[8] B. F. Spencer and S. Nagarajaiah, "State of the art of structural control," *Journal of Structural Engineering*, vol. 129, no. 7, pp. 845–856, 2003.

[9] T. T. Soong and M. C. Costantinou, *Passive and Active Structural Vibration Control in Civil Engineering*, Springer, New York, 1994.

[10] G. W. Housner, L. A. Bergman, T. K. Caughey et al., "Structural control: past, present, and future," *Journal of Engineering Mechanics*, vol. 123, no. 9, pp. 897–971, 1997.

[11] T. T. Soong and G. F. Dargush, *Passive Energy Dissipation Systems in Structural Engineering*, Wiley, 1997.

[12] R. W. K. Chan, F. Albermani, and S. Kitipornchai, "Experimental study of perforated yielding shear panel device for passive energy dissipation," *Journal of Constructional Steel Research*, vol. 91, no. 2, pp. 14–25, 2013.

[13] M. D. Symans, F. A. Charney, A. S. Whittaker et al., "Energy dissipation systems for seismic applications: current practice and recent developments," *Journal of Structural Engineering*, vol. 134, no. 1, pp. 3–21, 2008.

[14] M. M. Javidan, S. Chun, and J. Kim, "Experimental study on steel hysteretic column dampers for seismic retrofit of structures," *Steel and Composite Structures*, vol. 40, no. 4, pp. 495–509, 2021.

[15] H. Wijaya, P. Rajeev, E. Gad, and A. Amirsardari, "Effect of hysteretic steel damper uncertainty on seismic performance of steel buildings," *Journal of Constructional Steel Research*, vol. 157, no. 5, pp. 46–58, 2019.

[16] M. Latour, V. Piluso, and G. Rizzano, "Experimental analysis of beam-to-column joints equipped with sprayed aluminium friction dampers," *Journal of Constructional Steel Research*, vol. 146, no. 3, pp. 33–48, 2018.

[17] S. Veismoradi, S. M. M. Yousef-beik, P. Zarnani, and P. Quenneville, "Development and parametric study of a new self-centering rotational friction damper," *Engineering Structures*, vol. 235, Article ID 112097, 2021.

[18] Z. D. Xu, D. X. Wang, and C. F. Shi, "Model, tests and application design for viscoelastic dampers," *Journal of Vibration and Control*, vol. 17, no. 9, pp. 1359–1370, 2011.
[19] H. N. Li, X. Fu, Y. L. Li, and H. J. Liu, "Mechanical model and structural control performance of a new rotation-magnified viscoelastic damper," *Engineering Structures*, vol. 252, Article ID 113569, 2022.
[20] J. M. Kelly, R. I. Skinner, and A. J. Heine, "Mechanisms of energy absorption in special devices for use in earthquake resistant structures," *Bulletin of the New Zealand Society for Earthquake Engineering*, vol. 5, no. 3, pp. 63–88, 1972.
[21] A. S. Whittaker, V. V. Bertero, C. L. Thompson, and L. J. Alonso, "Seismic testing of steel plate energy dissipation devices," *Earthquake Spectra*, vol. 7, no. 4, pp. 563–604, 1991.
[22] R. K. Mohammadi, A. Nasri, and A. Ghaffary, "TADAS dampers in very large deformations," *International Journal of Steel Structures*, vol. 17, no. 2, pp. 515–524, 2017.
[23] J. H. Gao, J. H. Xi, Y. W. Xu et al., "Analysis of the mechanical properties and parameter sensitivity of a U-shaped steel damper," *Frontiers in Materials*, vol. 8, 2021.
[24] Z. P. Zhai, W. Guo, Z. W. Yu, C. J. He, and Z. Zeng, "Experimental and numerical study of S-shaped steel plate damper for seismic resilient application," *Engineering Structures*, vol. 221, Article ID 111006, 2020.
[25] R. W. K. Chan and F. Albermani, "Experimental study of steel slit damper for passive energy dissipation," *Engineering Structures*, vol. 30, no. 4, pp. 1058–1066, 2008.
[26] C. Quan, W. Wang, Y. Li, and Z. Lu, "Cyclic behaviour of demountable metallic corrugated shear panel dampers," *Journal of Building Engineering*, vol. 61, Article ID 105228, 2022.
[27] Z. Dongbin, N. Xin, P. Peng, W. Mengzi, D. Kailai, and C. Yabin, "Experimental study and finite element analysis of a buckling-restrained brace consisting of three steel tubes with slotted holes in the middle tube," *Journal of Constructional Steel Research*, vol. 124, no. 1, pp. 1–11, 2016.
[28] E. Montazeri, S. M. Kazemi, and S. S. Askariani, "Finite element parametric study on the cyclic response of steel frames equipped with comb-teeth dampers," *Structures*, vol. 31, pp. 111–126, 2021.
[29] M. Ahmadi and M. E. Jamkhaneh, "Seismic upgrading of existing steel buildings built on soft soil using passive damping systems," *Buildings*, vol. 13, no. 7, p. 1578, 2023.
[30] M. Ahmadi and M. Ebadi Jamkhaneh, "Numerical investigation of energy dissipation device to improve seismic response of existing steel buildings with soft-first-story," *International Journal of Steel Structures*, vol. 21, no. 2, pp. 691–702, 2021.
[31] V. Garmeh, A. Akbarpour, M. Adibramezani, A. Hojat Kashani, and M. Adibi, "Introducing and numerical study of an innovative rotational damper with replaceable hourglass steel pins," *Structures*, vol. 33, no. 145, pp. 2019–2035, 2021.
[32] M. Khalili, A. Sivandi-Pour, and E. Noroozinejad Farsangi, "Experimental and numerical investigations of a new hysteretic damper for seismic resilient steel moment connections," *Journal of Building Engineering*, vol. 43, Article ID 102811, 2021.
[33] B. H. Dai, Y. L. Gao, Z. Tao, H. H. Su, and H. X. Su, "Fan-shaped shear dampers strengthen mortise-tenon joints in Chinese traditional timber structures," *International Journal of Architectural Heritage*, vol. 17, no. 7, pp. 1079–1092, 2023.
[34] H. N. Li, Z. Huang, and X. Fu, "Study on the performance of a gear-driven rotation-amplified rubber viscoelastic damper and its vibration control of a frame structure," *Structural Control and Health Monitoring*, vol. 27, no. 11, pp. 28–51, 2020.
[35] M. Ye, J. Jiang, J. Y. Zhou, W. Zhang, B. Huang, and M. Wu, "Seismic mitigation effect of lever-type lead viscoelastic node dampers," *Structural Control and Health Monitoring*, vol. 2023, pp. 1–22, 2023.
[36] J. Z. Wang, K. Liu, A. Li, K. Dai, Y. Yin, and J. Li, "Shaking table test of a 1:10 scale thermal power plant building equipped with passive control systems," *Engineering Structures*, vol. 232, Article ID 111804, 2021.
[37] J. Z. Wang, K. S. Dai, Y. X. Yin, and S. Tesfamariam, "Seismic performance-based design and risk analysis of thermal power plant building with consideration of vertical and mass irregularities," *Engineering Structures*, vol. 164, pp. 141–154, 2018.
[38] M. Baiguera, G. Vasdravellis, and T. L. Karavasilis, "Dual seismic-resistant steel frame with high post-yield stiffness energy-dissipative braces for residual drift reduction," *Journal of Constructional Steel Research*, vol. 122, pp. 198–212, 2016.
[39] Fema, "Interim testing protocols for determining the seismic performance characteristics of structural and nonstructural components," *Ambio: Appl Technol Council*, 2000.
[40] H. N. Li, X. Fu, Y. L. Li, and H. J. Liu, "Mechanical model and structural control performance of a new rotation-magnified viscoelastic damper," *Engineering Structures*, vol. 252, Article ID 113569, 2022.
[41] Y. L. Shen, C. Christopoulos, N. Mansour, and R. Tremblay, "Seismic design and performance of steel moment-resisting frames with nonlinear replaceable links," *Journal of Structural Engineering*, vol. 137, no. 10, pp. 1107–1117, 2011.
[42] Abaqus, *User Manual*, SIMULIA World Headquarters, Providence, 2020.
[43] S. W. Han, J. Hyun, E. Cho, and K. Lee, "Efficient determination of combined hardening parameters for structural steel materials," *Steel and Composite Structures*, vol. 42, no. 5, pp. 657–669, 2022.
[44] H. C. Yang, W. Zhang, X. C. Zhuang, and Z. Zhao, "Calibration of chaboche combined hardening model for large strain range," *Procedia Manufacturing*, vol. 47, pp. 867–872, 2020.